Ground-Motion Amplification in Cook Inlet Region, Alaska, from Intermediate-Depth Earthquakes, Including the 2018 M_w 7.1 Anchorage Earthquake

Morgan P. Moschetti*[1], Eric M. Thompson[1], John Rekoske[1], Michael G. Hearne[1], Peter M. Powers[1], Daniel E. McNamara[1], and Carl Tape[2]

Abstract

We measure pseudospectral and peak ground motions from 44 intermediate-depth $M_w \geq 4.9$ earthquakes in the Cook Inlet region of southern Alaska, including those from the 2018 M_w 7.1 earthquake near Anchorage, to identify regional amplification features (0.1–5 s period). Ground-motion residuals are computed with respect to an empirical ground-motion model for intraslab subduction earthquakes, and we compute bias, between-, and within-event terms through a linear mixed-effects regression. Between-event residuals are analyzed to assess the relative source characteristics of the Cook Inlet earthquakes and suggest a difference in the scaling of the source with depth, relative to global observations. The within-event residuals are analyzed to investigate regional amplification, and various spatial patterns manifest, including correlations of amplification with depth of the Cook Inlet basin and varying amplifications east and west of the center of the basin. Three earthquake clusters are analyzed separately and indicate spatial amplification patterns that depend on source location and exhibit variations in the depth scaling of long-period basin amplification. The observations inform future seismic hazard modeling efforts in the Cook Inlet region. More broadly, they suggest a greater complexity of basin and regional amplification than is currently used in seismic hazard analyses.

Cite this article as Moschetti, M. P., E. M. Thompson, J. Rekoske, M. G. Hearne, P. M. Powers, D. E. McNamara, and C. Tape (2019). Ground-Motion Amplification in Cook Inlet Region, Alaska, from Intermediate-Depth Earthquakes, Including the 2018 M_w 7.1 Anchorage Earthquake, *Seismol. Res. Lett.* **91**, 142–152, doi: 10.1785/0220190179.

Supplemental Material

Introduction

The 30 November 2018 M_w 7.1 earthquake near Anchorage, Alaska, exposed more than 270,000 people to very strong shaking (modified Mercalli intensity [MMI] ≥ VII) and highlighted the ground-shaking hazards associated with intermediate-depth (intraslab) earthquakes in the Cook Inlet region (Earle *et al.*, 2009; Franke *et al.*, 2018). Because of their relatively higher recurrence rates and enhanced shaking levels, compared to equivalent-magnitude events on the subduction interface, intermediate-depth earthquakes make significant contributions to probabilistic seismic hazard analyses in Anchorage, as well as to other U.S. urban areas near subduction zones (e.g., Wesson *et al.*, 2007; Abrahamson *et al.*, 2014; Frankel *et al.*, 2015; M. D. Petersen *et al.*, unpublished manuscript, 2019, see Data and Resources).

The modification and amplification of earthquake ground motions by local geologic structure are widely recognized (e.g., Borcherdt, 1970; Aki, 1993). These include effects caused by the thickness and wavespeeds of soils and sedimentary basins, topography, and wave propagation, such as focusing and interference, among others (e.g., Geli *et al.*, 1988; Anderson *et al.*, 1996; Davis *et al.*, 2000; Frankel *et al.*, 2002). Our analysis focused on the Cook Inlet, which overlies a fore-arc basin with sedimentary thicknesses of up to about 7.4 km (Fig. 1). The presence of a deep sedimentary basin and a broad, regional distribution of earthquakes also permitted investigation of basin and site effects from different earthquake clusters.

Ground-motion observations and simulations indicate large amplifications and complications of the seismic wavefield by sedimentary basins, particularly at long periods ($T \gtrsim 1$ s) (e.g., Frankel, 1993; Kawase, 1996; Hartzell *et al.*, 1997; Olsen, 2000; Feng and Ritzwoller, 2017; Moschetti *et al.*, 2017; Frankel *et al.*, 2018; Wirth, Frankel, *et al.*, 2018). Empirical ground-motion models (GMMs), which are most commonly used for

1. Geologic Hazards Science Center, U.S. Geological Survey, Denver, Colorado, U.S.A.; 2. Geophysical Institute, University of Alaska Fairbanks, Fairbanks, Alaska, U.S.A.

*Corresponding author: mmoschetti@usgs.gov

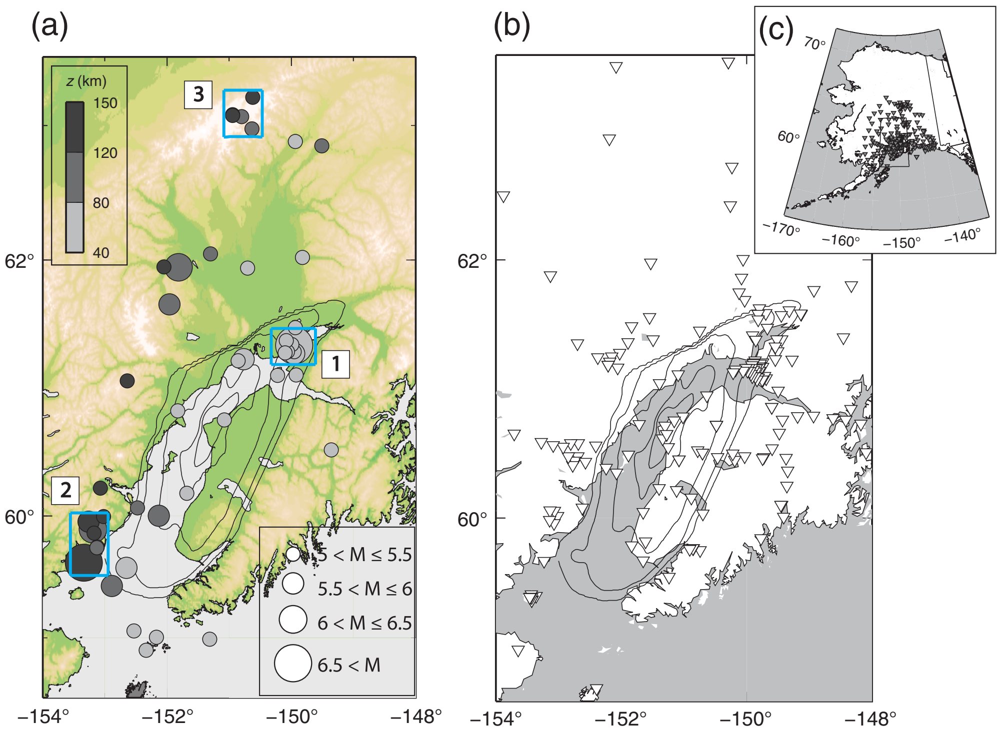

Figure 1. Map of (a) earthquake epicenters and (b,c) station locations. (a) Focal depths and magnitudes are depicted by shade and symbol size, respectively. Blue rectangles identify three earthquake clusters: (1) Anchorage, (2) Augustine, and (3) Denali. Contours depict the 100, 1000, 3000, 5000, and 6000 m depths to basement from Shellenbaum *et al.* (2010).

probabilistic and deterministic seismic hazard analyses, employ depths to shear-wave velocity horizons of 1.0 and 2.5 km/s—referred to as Z1.0 and Z2.5, respectively—to model the scaling of basin amplification with sediment thickness (e.g., Abrahamson *et al.*, 2014; Campbell and Bozorgnia, 2014). Although these models capture the average amplification features depicted in ground-motion databases, they do not predict complicated wave propagation features, discriminate between the phases controlling strong motions at a site, or differentiate between regional variations in basin structure, depths, and seismic velocities, all of which have been demonstrated to affect earthquake ground motions (e.g., Choi *et al.*, 2005; Frankel *et al.*, 2009; Denolle *et al.*, 2014; Bowden and Tsai, 2017; Nweke *et al.*, 2018; Wirth *et al.*, 2019). In a parallel effort, Smith and Tape (2019) analyzed earthquake ground motions and ambient seismic noise levels to investigate the seismic response of the Cook Inlet basin.

In this article, ground motions from the M_w 7.1 Anchorage, Alaska, earthquake and from other intermediate-depth earthquakes occurring in the vicinity of Cook Inlet are analyzed to investigate basin amplification and regional site effects by partitioning ground-motion features into their constituent site and source effects. In addition to average amplification effects, we examined ground motions from three earthquake clusters to investigate the variations in basin response and site amplification from different source regions.

Methods

Ground-motion processing

We developed a catalog of intermediate-depth earthquakes affecting upper Cook Inlet, occurring between 1 January 2008 and 1 March 2019, by selecting events from the U.S. Geological Survey (USGS) comprehensive earthquake catalog (ComCat; Guy *et al.*, 2015) for earthquakes within 300 km of Anchorage. We identify intermediate-depth earthquakes—defined for our study as those events occurring within the subducted slab and at depths greater than the subduction interface—by applying the scheme of Garcia *et al.* (2012) and slab depth contours (Hayes *et al.*, 2018). We did not include earthquakes that may have been active crustal events and permitted events with probabilities of intraslab character of greater than 25%. The catalog was limited to events $M_w \geq 4.9$ so that we could compare recorded ground motions to current model predictions with minimal extrapolation of the magnitude scaling terms (Abrahamson *et al.*, 2016). The resulting catalog contains 44 earthquakes, occurring beneath Cook Inlet and extending to the Alaska range (Fig. 1), with depths ranging 35–144 km and magnitudes ranging M_w 7.1.

For all events in the earthquake catalog, we collected three-component seismic waveforms from instruments with epicentral distances less than 300 km. Data were obtained from the Incorporated Research Institutions for Seismology (IRIS) Data Management Center and from the Center for Engineering Strong-Motion Data (CESMD) (see Data and Resources). Processing of the time series and ground motions followed standard strong-motion procedures (e.g., Ancheta *et al.*, 2014; Goulet *et al.*, 2014; Rennolet *et al.*, 2018). Waveforms were obtained from strong-motion and broadband instruments from permanent networks, USArray Transportable Array, and temporary deployments, including Multidisciplinary Observations Of Subduction (Li *et al.*, 2013), Southern Alaska Lithosphere and Mantle Observation Network (Tape *et al.*, 2017), and a

USGS aftershock deployment installed in response to the 2018 Anchorage earthquake. We did not include data from strong-motion instruments located in structures (e.g., Çelebi, 2006, 2019). Waveforms were demeaned and detrended, assessed for clipping—through count exceedance of the raw traces (e.g., Rennolet *et al.*, 2018)—instrument-response corrected, and windowed using *P*-wave phase arrival times from a 1D seismic velocity model (Kennett and Engdahl, 1991). Band-pass filtering employed filter corners that were dynamically selected to ensure that signal-to-noise ratios exceeded three in the passband. An additional baseline correction to the displacement time series was made by fitting a sixth-order polynomial to the displacement waveforms, constrained such that the zero- and first-order terms were zero (e.g., Ancheta *et al.*, 2014), and then removing the second derivative of the polynomial from the acceleration time series.

Peak ground accelerations, peak ground velocity, and 5%-damped pseudospectral accelerations (SAs) for oscillator periods (0.1–10 s) were computed from the horizontal-component waveforms and combined using the rotation-independent intensity measure, RotD50, which combines separate measurements from the horizontal-component waveforms (Boore, 2010). Ground-motion processing was carried out with the open-source gmprocess Python-based package (Hearne *et al.*, 2019), which builds on previous code base, has been validated against ground motions in the Next Generation Attenuation-West2 Project (NGA-West2) flatfile, and uses various seismic processing features from ObsPy (e.g., Ancheta *et al.*, 2014; Krischer *et al.*, 2015; Rennolet *et al.*, 2018; Thompson *et al.*, 2019). The resulting database contains 2925 records. Record density for moderate-size earthquakes ($4.9 \lesssim M_w < 5.75$) is good at all distances, sparse for magnitudes $5.75 \lesssim M_w < 6.5$, primarily at regional distances (Fig. S1, available in the supplemental material to this article); there are no records for $6.5 \lesssim M_w < 7$ earthquakes, although record density from earthquakes $M_w \geq 7$ is good for epicentral distances less than 50 km, largely due to the high instrument density in Anchorage and its proximity to the M_w 7.1 earthquake, and moderate for larger distances.

Ground-motion residuals

Analysis of ground-motion residuals followed procedures from previous studies (e.g., Thompson and Wald, 2016; Moschetti *et al.*, 2018). Ground-motion predictions were computed from Abrahamson *et al.* (2016) using the slab variant and without accounting for attenuation differences between fore-arc and back-arc sites $\ln(\mathrm{SA}_{es}^{\mathrm{GMM}})$. McNamara *et al.* (2019) recently demonstrated that, on average, Abrahamson *et al.* (2016) accurately reproduce the recorded ground motions for the M_w 7.1 Anchorage earthquake and its aftershocks. Total ground-motion residuals R_{es} were computed for all events e and sites s, using V_{S30} values from a topography-based proxy (Wald and Allen, 2007):

$$R_{es} = \ln(\mathrm{SA}_{es}) - \ln(\mathrm{SA}_{es}^{\mathrm{GMM}}). \quad (1)$$

Intraslab ground motions in the Abrahamson *et al.* (2016) GMM exhibit period-dependent depth scaling, which is implemented as a source term. For increasing focal depths, SA increases for periods less than 5 s and decreases for longer periods. These trends saturate for focal depths of 120 km.

We decomposed the total residuals into between-event δB_e and within-event δW_{es} terms, and a bias term c, using a linear mixed-effects regression (Al Atik *et al.*, 2010; Pinheiro *et al.*, 2013):

$$R_{es} = \delta B_e + \delta W_{es} + c. \quad (2)$$

Constrained by mean values:

$$\langle \delta B_e \rangle = 0, \quad (3)$$

$$\langle \delta W_{es} \rangle_s = 0. \quad (4)$$

Our presentation focuses on a representative oscillator period set: 0.1, 0.3, 1.0, and 3.0 s.

The presence of spatially clustered earthquakes permitted us to aggregate the residual terms (equation 2) to better understand effects of seismic-wave amplification in the Cook Inlet region from different sources regions. In addition to the results from all earthquakes, we analyzed results from three earthquake clusters (Fig. 1)—(1) the M_w 7.1 Anchorage earthquake ($z = 46$ km) and its aftershocks (Anchorage cluster); (2) a cluster of deep ($z > 100$ km) earthquakes west of Homer, near Augustine Island (Augustine cluster); and (3) a cluster of deep ($z > 100$ km) earthquakes beneath the Alaska range and north of the Susitna valley (Denali cluster). Data coverage of Cook Inlet basin is greater for the Anchorage cluster due to the large number of aftershocks and the deployment of temporary seismometers that recorded many events from this cluster.

Sediment thicknesses in Cook Inlet basin and empirical basin amplification

The Abrahamson *et al.* (2016) GMM does not include terms that amplify ground motions for the effects from deep sediments. Although separating the contributions to amplification from the shallow (i.e., V_{S30}) and deeper parts of the seismic velocity profile is nonunique, V_{S30} has been demonstrated to negatively correlate with basin depths in some regions. For example, Nweke *et al.* (2018) indicate increasing Z1 values for decreasing V_{S30}, for a data set from southern California. As a consequence, some effects of basin amplification may be captured by the GMM site response models. However, we investigated basin effects by examining trends in ground-motion residuals with the sediment depths in the Cook Inlet basin (Shellenbaum *et al.*, 2010). We interpreted the depths to the top of the Mesozoic unconformity (Shellenbaum *et al.*, 2010) to correspond to Z2.5, consistent with guidance from Campbell and Bozorgnia (2014).

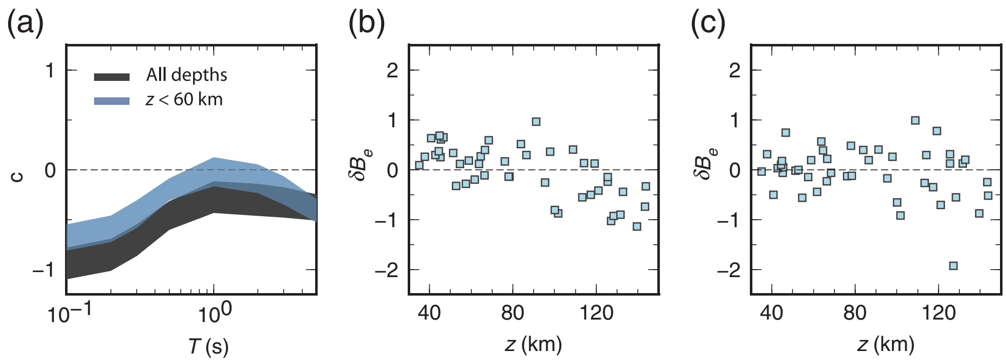

Figure 2. Representation of average bias and event terms based on 44 earthquakes recorded in the Cook Inlet region. (a) 95% confidence intervals for bias terms c plotted as a function of oscillator period. This term corresponds to the average difference—over all ground-motion recordings—between the Abrahamson *et al.* (2016) predictions and the recorded ground motions, at each period. Bias terms from all earthquakes and from earthquakes with focal depths less than 60 km are plotted in black and cyan, respectively. (b) Between-event δB_e terms, plotted as a function of event depth, for 0.3 s oscillator period. This term corresponds to the average deviation of ground motions from each event, from the mean model. (c) Same as (b) but for 3.0 s oscillator period.

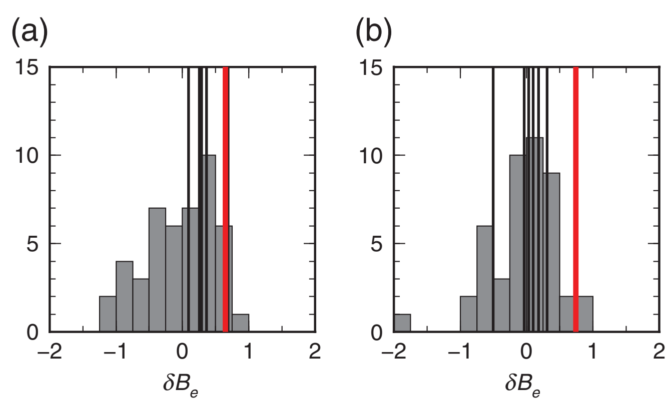

Figure 3. Histograms of between-event terms δB_e at oscillator periods of (a) 0.3 and (b) 3.0 s. Red and black lines overlay the histogram and depict the between-event terms from the Anchorage M_w 7.1 earthquake and its aftershocks.

Empirical basin amplifications were computed from the four NGA-West2 GMMs for comparison with the observed basin amplifications (Abrahamson *et al.*, 2014; Boore *et al.*, 2014; Campbell and Bozorgnia, 2014; Chiou and Youngs, 2014). These empirical amplification models were developed from the NGA-West2 database (Ancheta *et al.*, 2014) and are constrained by data and 3D ground-motion simulations from southern California (e.g., Day *et al.*, 2008). We computed equivalent Z1 values from the estimated Z2.5 values using the regression equations of M. D. Petersen *et al.* (unpublished manuscript, 2019, see Data and Resources). Basin amplifications describe the sediment-depth dependence of the linear contributions to the mean ground-motion predictions.

Results

Bias and between-event terms

For longer periods ($T \gtrsim 1$ s) and focal depths less than about 100 km, Abrahamson *et al.* (2016) agree with the ground motions in our data set (Fig. 2a). However, the GMM overpredicts ground motions at shorter periods and greater focal depths, and the bias and between-event terms indicate an increasing overprediction with increasing focal depth. Bias is particularly acute at the shortest oscillator periods ($T \lesssim 0.5$ s) (Fig. 2a). At long periods ($T > 5$ s), mean bias corresponds to about a 20% underprediction, and bias is minimized near 1 s period. Carrying out the mixed-effects regression for shallower events ($z < 60$ km) indicates that deeper events contribute to much of the overall bias; however, a similar period-dependence remains in the bias terms, although shifted closer to zero.

Between-event terms are anticorrelated with depth, and the anticorrelations are stronger for shorter periods ($T \lesssim 1$ s) and weak to negligible at long periods (Fig. 2b,c and Fig. S2). A correlation between magnitude and between-event terms appears to manifest in the data, possibly with increasing correlation at long periods ($T \geq 1$ s) (Fig. S3). However, there are too few larger magnitude ($M_w \geq 6$) records to make a definitive conclusion. Between-event terms from the Anchorage cluster range $0 < \delta B_e \lesssim 0.75$ for all periods, with the between-event term from the M_w 7.1 earthquake exceeding those from all aftershocks in the cluster, except for the term from one aftershock at 1.0 s period (Fig. 3 and Fig. S4). Because the mixed-effects regression is constrained to find between events with a zero mean value, the bias term also contains information about errors in the absolute ground-motion level (and region-wide amplification factors). Summing the bias and between-event residuals from the Anchorage cluster (Fig. S5), we found that absolute values of the combined residuals ($c + \delta B_e$) are less than about 0.4 and show a positive correlation with period.

Although the bias and between-event residuals exhibit systematic misfits, these features are separated from the within-event residuals by the mixed-effects regression, and our analysis of the within-event terms presumes an independence from source effects. Because of the strong anticorrelation between event depth and the between-event terms, we computed the Pearson correlation coefficient between event depths and basin depths to evaluate the potential for source effects to produce

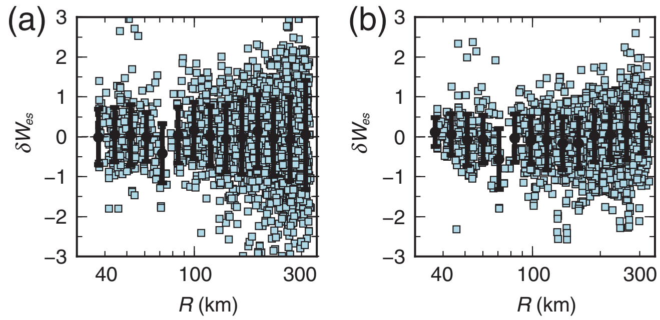

Figure 4. Within-event terms δW_{es}, plotted as a function of hypocentral distance R for oscillator periods (a) 0.3 and (b) 3.0 s. Positive values indicate greater than average site amplification. Cyan squares depict all within-event terms, and the black error bars depict one standard deviation from the mean.

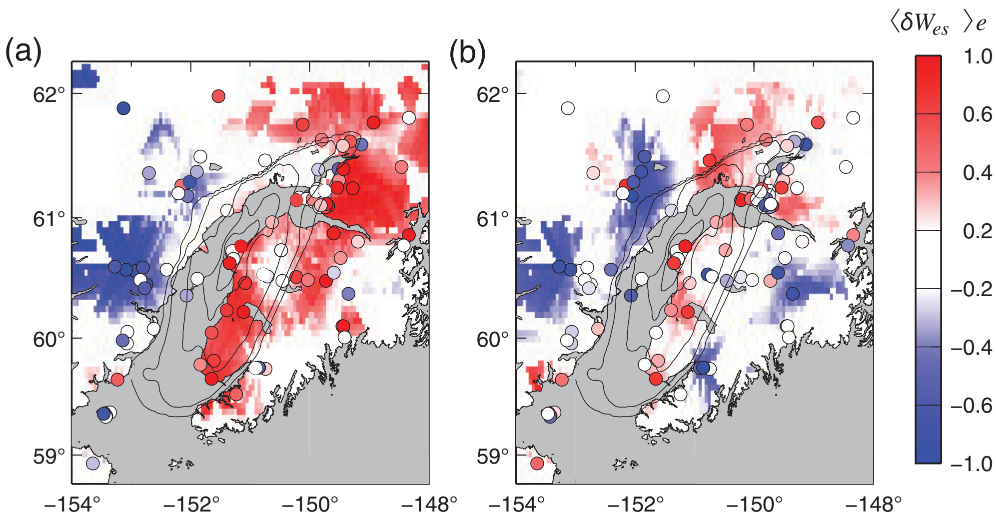

Figure 5. Mean site residuals $\langle \delta W_{es} \rangle_e$ are plotted for oscillator periods (a) 0.3 and (b) 3.0 s. Symbols and background colors depict $\langle \delta W_{es} \rangle_e$ at sites and from spatially smoothed values, respectively. Contours depict the 100, 1000, 3000, 5000, and 6000 m depths to basement from Shellenbaum *et al.* (2010).

artifacts in the basin analyses. We found $\rho = -0.029$ ($p = 0.125$), indicating no correlation between the basin and event depths. Although there is significant scatter in the within-event terms, the mean, binned ground motions are near-zero across the hypocentral distance range, up to 300 km (Fig. 4 and Fig. S6), indicating good distance scaling of the GMM. The near-zero average trend of the within-event terms with distance minimizes concern that incorrect modeling of path attenuation will map into distance-dependent site effects.

Regional amplification features

We investigate amplification patterns through a mean site-residual parameter $\langle \delta W_{es} \rangle_e$, which averages the within-event residuals, at each site, over all events. Mean site residuals exhibit spatial clustering patterns that vary with period (Fig. 5 and Fig. S7). Spatial patterns are highlighted by spatially smoothing the mean site residuals using a nearest-neighbor algorithm that requires observations in three of eight azimuthal sectors and uses observations within 50 km epicentral distance (Wessel *et al.*, 2013). At shorter periods (0.1 and 0.3 s), negative residuals ($\langle \delta W_{es} \rangle_e < 0$) manifest west of Cook Inlet; residuals within the basin tend to be positive but do not present strong correlations with basin depths; and residuals north and east part of the basin are predominantly high ($\langle \delta W_{es} \rangle_e > 0.5$). A similar spatial pattern, although with reduced amplitudes and negative residuals on the eastern Kenai Peninsula, manifests at longer periods (1.0 and 3.0 s).

Comparisons of the within-event residuals and basin depth indicate that ground motions at all periods are amplified by the Cook Inlet basin and that the amplification of longer period ($T \gtrsim 0.5$ s) ground motions correlate with basin depth. Average depth trends are illuminated by the mean and standard deviation in 20 logarithmically spaced basin-depth bins, ranging 50–10,000 m (Fig. 6 and Fig. S8). At shorter periods (0.1 and 0.3 s), the residuals are positive for nearly all basin depths ($\delta W_{es} \approx 0.5$) but show weak to no correlation with basin depth. Long-period (e.g., 1.0 and 3.0 s) residuals show a strong correlation with basin depth. Differences in the binned within-event residuals from the deep ($d > 1000$ m) and shallowest sites ($d < 200$ m) correspond to linear amplifications of more than two for periods ($0.5 \le T \le 5$ s), with a maximum amplification near 1 s period (Fig. 6d). The long-period residuals are comparable with the empirical basin amplifications from the NGA-West2 GMMs, which were computed for sites with $V_{S30} = 500$ m/s and $V_{S30} = 260$ m/s, whereas the trends we observe at shorter periods are not captured by these models.

Earthquake-cluster amplifications

We investigated how site amplification differs between different earthquake clusters through an earthquake-cluster amplification factor $\mathrm{AF}_{s,\mathrm{Cl}}$:

$$\mathrm{AF}_{s,\mathrm{Cl}} = \langle \delta W_{es} \rangle_{e \in \mathrm{Cl}} - \langle \delta W_{es} \rangle_e. \quad (5)$$

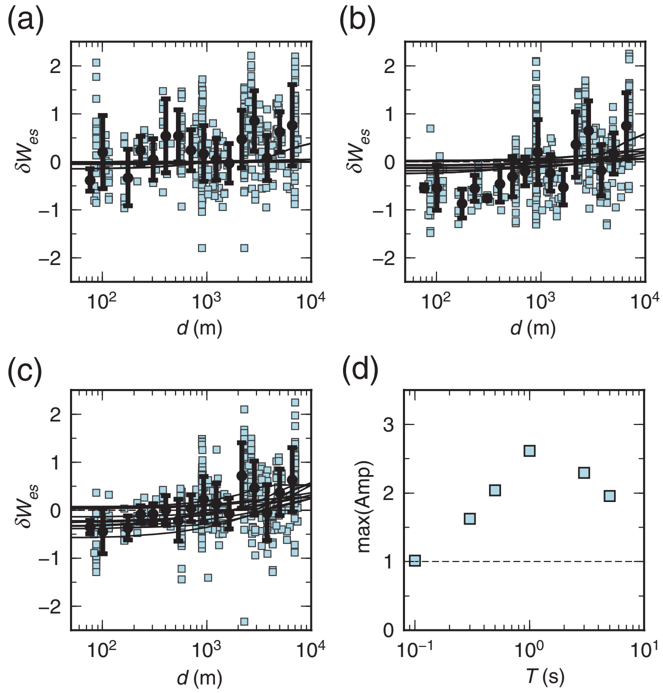

Figure 6. Within-event terms δW_{es} from all earthquakes, plotted as a function of basin depth, at oscillator periods (a) 0.3, (b) 1.0, (c) 3.0 s, and (d) maximum (linear) amplifications plotted as a function of period T. Cyan squares depict all within-event terms, and black error bars depict standard deviations computed for logarithmically spaced basin depth bins. Thin, black lines depict empirical basin amplifications from Next Generation Attenuation-West2 Project (NGA-West2) ground-motion models (GMMs).

The cluster amplification factors $AF_{s,Cl}$ represent the difference between site amplification caused by an earthquake cluster and the site amplification determined by averaging over all earthquakes. Sites that experience higher average within-event residuals from an earthquake cluster (than the average from all earthquakes) have $AF_{s,Cl} > 0$, and we refer to the sites as being amplified by a particular cluster; sites that experience lower within-event residuals from an earthquake cluster have $AF_{s,Cl} < 0$, and we refer to the sites as being deamplified by the cluster.

Spatial coverage of the cluster amplification factors $AF_{s,Cl}$ differs because of the distances of the three earthquake clusters from Cook Inlet basin and the restriction of the ground motion processing to 300 km epicentral distances. As a consequence, cluster amplification factors from the Anchorage and Augustine clusters span the Cook Inlet basin, whereas those from the Denali cluster only span the northern part of the basin.

Earthquake-cluster amplification factors $AF_{s,Cl}$ show coherent spatial patterns at all periods, with values ranging from about −1 to 1 (Fig. 7 and Fig. S9). Short-period (0.1, 0.3 s) amplification from the Anchorage and Augustine clusters is highly anticorrelated. The Anchorage cluster amplifies ($AF_{s,Cl} > 0$) ground motions on the distant, west side of Cook Inlet and deamplifies ground motions in the vicinity of the earthquakes. Ground motions in the northeast part of Cook Inlet are amplified by the Augustine cluster, and they are deamplified west of the epicentral region. These amplification factors are reduced at 1.0 s period and greatly minimized by 3.0 s period.

Amplification factors from the Denali cluster exhibit near-uniform amplification at short periods, although measurements are limited to the northeastern reach of Cook Inlet. At longer periods, spatial amplification patterns, from the Denali cluster, show relative amplification within the basin.

The three clusters also exhibit different scaling of the within-event residuals with basin depth (Fig. 8, and Figs. S10 and S11). Short-period (0.1, 0.3 s) within-event terms show weak scaling with basin depth. Within-event residuals from the Anchorage cluster are near-zero and suggest weak scaling at the sites overlying the largest basin depths. The within-event terms from the Augustine and Denali clusters have high variability but are centered near ~1.0, suggesting that these clusters result in average amplifications within the basin of more than a factor of 2.5.

Long-period (1.0, 3.0 s) within-event terms correlate with basin depth. Scaling is the weakest for the Anchorage cluster, intermediate for the Augustine cluster, and strongest for the Denali cluster. Within-event terms from the Anchorage cluster nearly track the empirical amplification factors at all basin depths. Within-event terms from the Augustine cluster exhibit similar, but greater, basin amplification; the within-event terms at the largest basin depths ($z > 1000$ m) exceed the empirical basin amplifications by about 0.25, corresponding to an additional amplification of more than 25%. Scaling of the within-event terms with basin depth from the Denali cluster far surpasses the empirical basin amplifications. Within-event terms at sites overlying the largest basin depths ($z > 1000$ m) exceed the empirical basin amplifications by more than 0.5, which corresponds to additional amplification of more than 60%. In addition, sites with shallow sedimentary thicknesses ($z < 100$ m) are deamplified with respect to the empirical basin amplification models, by 50% or more. As a consequence, scaling of the within-event terms with basin depth is much stronger than in the empirical basin amplification models. Furthermore, ratios of the site residuals δW_{es} for basin depths greater than 1000 m to those with depths less than 200 m indicate that the three clusters all have maximum amplifications above 1 s period (Fig. S11)

Discussion

Between-event residuals and average bias terms indicate that the ground motions from intermediate-depth earthquakes examined in this study are lower, on average, than predicted by the global model of Abrahamson *et al.* (2016) GMM. Several factors likely contribute to this trend. First, we identified a persistent bias for shallower ($z < 60$ km) and deeper events, although this trend is strongest for focal depths greater than 120 km. These trends suggest that the absolute source levels or the depth scaling terms in Abrahamson *et al.* (2016) GMM are

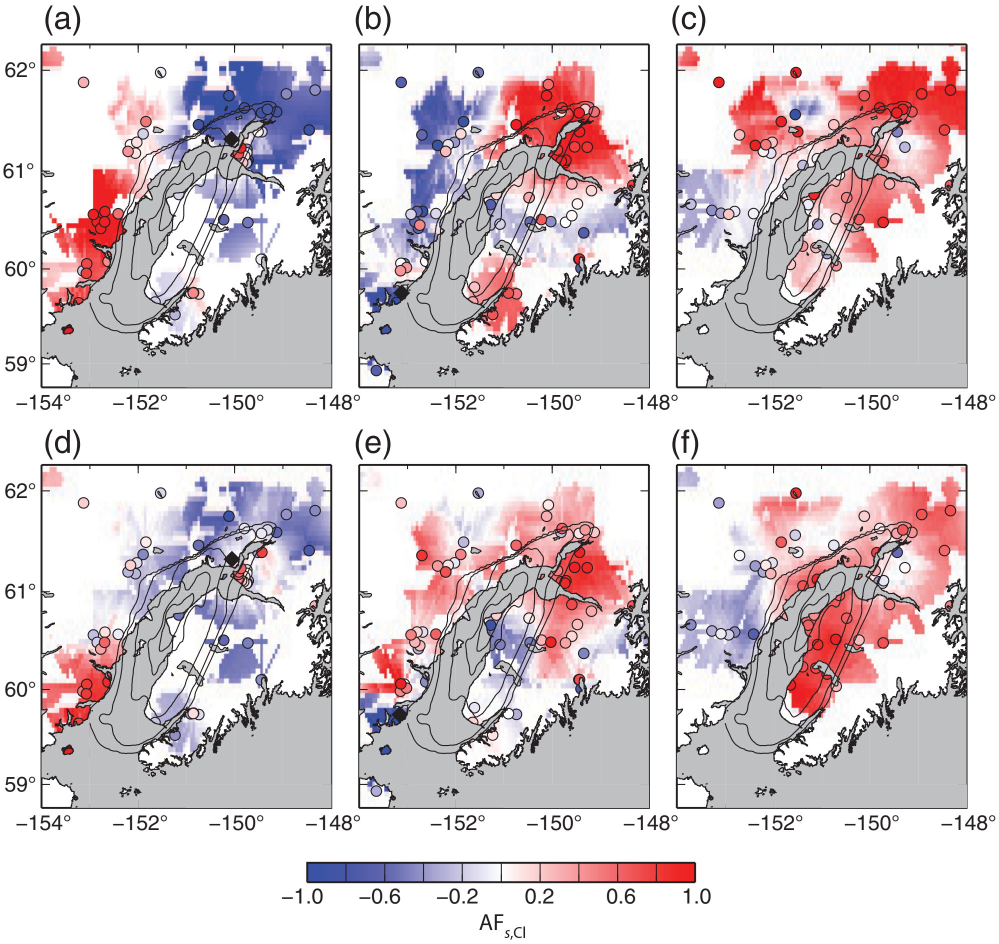

Figure 7. Earthquake-cluster amplification factors $AF_{s,Cl}$ at oscillator periods of (a–c) 0.3 and (d–f) 3.0 s. Symbols and background colors depict $AF_{s,Cl}$ at sites and from spatial smoothing of the $AF_{s,Cl}$ data, respectively. Amplification factors from the (a,d) Anchorage cluster, (b,e) Augustine cluster, and (c,f) Denali cluster are plotted separately. Contours depict the 100, 1000, 3000, and 5000 m depths to basement from Shellenbaum *et al.* (2010). Black diamonds depict location of (a,d) Anchorage and (b,e) Augustine earthquake clusters.

too high for this region. Furthermore, they indicate that source depth scaling extends beyond 120 km. Variations in the level and depth scaling of ground motions may relate to plate age and properties (e.g., Müller *et al.*, 2008) or rupture characteristics and require further investigation. Because neither seismological (e.g., Andrews, 1986) nor engineering seismological models (e.g., Abrahamson *et al.*, 2014, 2016) couple the source and site spectral characteristics, within the linear-response regime, we do not expect application of the GMM to events with depths greater than 120 km to affect our analysis of regional amplification. Second, we noted lower between-event terms from the aftershocks of the M_w 7.1 Anchorage earthquake and our incorporation of aftershocks in the regression analysis had the potential to bias the analyses because ground motions from mainshocks and aftershocks are commonly treated separately in GMMs (e.g., Wooddell and Abrahamson, 2014).

Between-event residuals are commonly interpreted to correspond to variations in stress drop (e.g., Bindi *et al.*, 2017). Because distance attenuation is well modeled by the Abrahamson *et al.* (2016) GMM, it minimizes the concern that errors in distance scaling residuals caused artifacts in the between-event residuals (e.g., Wooddell and Abrahamson, 2019). That the combined residuals $(c + \delta B_e)$ from the M_w 7.1 Anchorage earthquake are small, and within the interevent standard deviations of the GMM, suggest that stress drop from the M_w 7.1 earthquake is comparable with global averages for events with similar focal depths. The lower combined residuals of aftershocks in the Anchorage cluster suggest lower stress drops for the aftershocks of the M_w 7.1 Anchorage earthquake, as has previously been observed in other regions (e.g., Boyd *et al.*, 2017).

Regional amplification—revealed by within-event residuals—indicates scaling of the long-period ($T \gtrsim 0.5$ s) ground motions with basin depth and coherent spatial patterns, including a depth-invariant amplification of shorter period ground motions within the basin. Accurate ground-motion prediction in the Cook Inlet region must include basin effects. On average, the scaling of ground motions with basin depth is well modeled by the NGA-West2 empirical basin amplifications. This observation appears to differ from recent results from basins in the U.S. Pacific Northwest and southern California, which indicate highly regionalized basin responses and suggest that basin geometry and seismic velocity structure may impose unique character on period-dependent basin amplifications (e.g., Chang *et al.*, 2014; Nweke *et al.*, 2018; Wirth, Chang, *et al.*, 2018; M. D. Petersen *et al.*, unpublished manuscript, 2019, see Data and Resources). Our results are broadly consistent with the longer period (2–10 s) results of Smith and Tape (2019), which indicate amplification factors of about 3–6; intriguingly, they demonstrate that the spectral amplitude

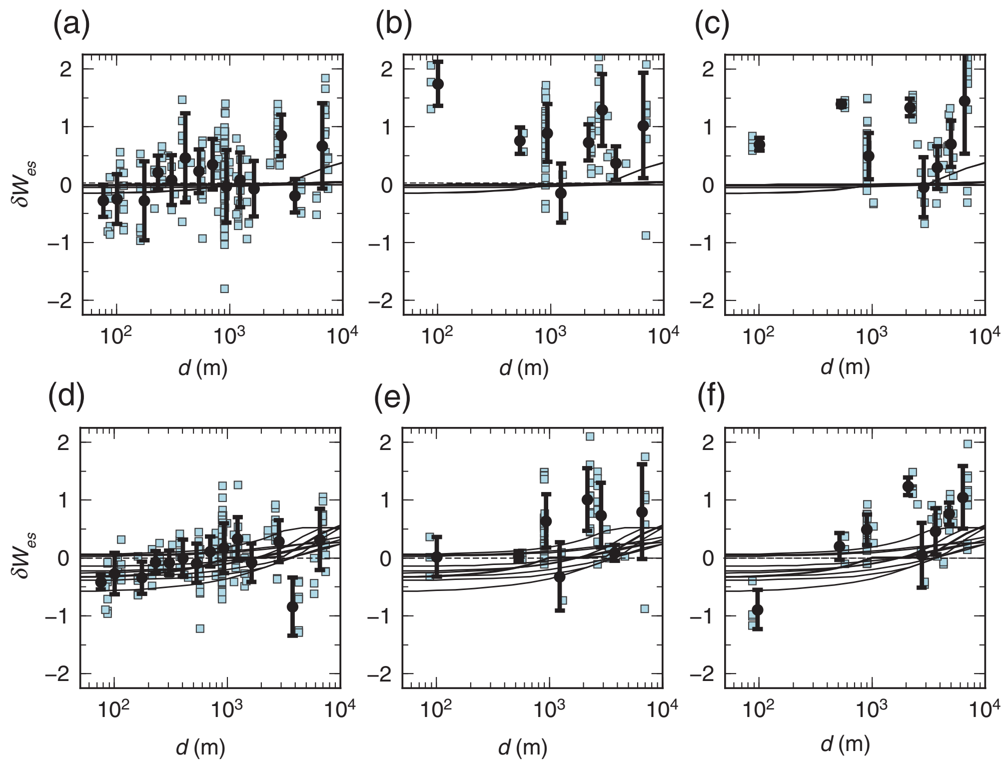

Figure 8. Within-event terms δW_{es} and mean-binned trends, plotted as a function of basin depth, at oscillator periods (a–c) 0.3 and (d–f) 3.0 s. Terms are plotted from the (a,d) Anchorage, (b,e) Augustine, and (c,f) Denali clusters. Cyan squares depict within-event terms from the individual earthquake clusters. Black error bars depict standard deviations computed for basin-depth bins from each cluster. Thin, black lines depict empirical basin amplifications from NGA-West2 GMMs.

ratios from ambient seismic noise and earthquake records, between basin and reference rock sites, largely agree.

Spatial patterns of the short-period site amplifications may arise because of regional focusing (e.g., Shapiro *et al.*, 2000) or local site amplifications. Because site response is highly sensitive to shallow site conditions, which can change rapidly over short spatial scales, detailed investigation of the short-period amplifications requires high-resolution site information. The short-period, depth-invariant basin amplification may result from improper characterization of the shallow site conditions (i.e., V_{S30}) or from regionalized, short-period site response that differs from the site response models that underlie Abrahamson *et al.* (2016). Detailed analysis of site response in the region requires additional information about local site conditions.

Analysis of three earthquake clusters reveals intriguing amplification features that vary between the clusters and manifest across a broad period band (~0.1–3.0 s), as well as variations in the scaling of long-period amplification with basin depth. The cause of the variations in ground-motion amplifications from the clusters is not yet understood. However, source-dependent spatial amplifications have previously been observed in earthquake records, ambient seismic noise analyses, and earthquake simulations (e.g., Frankel *et al.*, 2009; Denolle *et al.*, 2014; Wirth *et al.*, 2019); the amplifications may be caused by focusing and seismic-wave propagation features, contributions from different seismic phases, topography, or other mechanisms (e.g., Spudich *et al.*, 1996; Bowden and Tsai, 2017). Our observations also suggest that seismic-wave amplification by sedimentary basins may extend to shorter periods ($T \lesssim 1$ s) than are typically modeled (e.g., Abrahamson *et al.*, 2014).

Development of empirical basin amplification models for the Cook Inlet basin, and other regions, may need to consider more complicated basin response phenomena than are currently included in seismic hazard assessments. For example, depth scaling and spatial amplification patterns may depend on source regions. Because these variations in basin amplification effects represent additional uncertainty for the ground motions at sites within basins, they can also be formally treated in probabilistic seismic hazard analyses through modifications in the aleatory variability (e.g., Rodriguez-Marek *et al.*, 2014; Landwehr *et al.*, 2016). Ultimately, repeatable amplification effects should be incorporated into GMMs to increase their accuracy and reduce the associated uncertainty.

Conclusions

Ground motions from intermediate-depth earthquakes in the Cook Inlet region of Alaska were analyzed to investigate regional amplification features. The linear mixed-effects regression separates the ground-motion residuals, relative to the subduction zone GMM of Abrahamson *et al.* (2016), into source and site residuals. We identify a variation in the source scaling with event depth, relative to global averages, that may be due to the composition of our earthquake catalog, which includes aftershocks, or from regional variations in energy radiated from deeper earthquakes. Regional site amplifications identify spatially coherent patterns at all periods, including significant basin amplifications that scale with basin depth, and exhibit maximum amplifications of about a factor of 2 at 1 s period. Ground-motion amplifications vary with source location from three earthquake clusters and produce spatially coherent source-dependent amplifications across the period band 0.1–3 s; the correlations between basin depth and long-period ground motions exhibit significant differences from the three clusters, with the Anchorage cluster being well approximated by empirical basin amplification models developed for active crustal earthquakes, but the amplifications from the Augustine and Denali clusters are underpredicted by these empirical models. These observations motivate further investigation of ground-motion features in southcentral Alaska and support incorporation of basin amplification effects in earthquake hazards products for the Cook Inlet region.

Data and Resources

Waveform data used in this study can be accessed from the Incorporated Research Institutions for Seismology (IRIS) Data Management Center and the Center for Engineering Strong-Motion Data (CESMD). The supplemental material provides a list of all seismic networks contributing data for the ground-motion measurements in Table S1. The database of ground motions is available at Rekoske *et al.* (2019). Ground-motion processing used the gmprocess code (Hearne *et al.*, 2019). Ground-motion predictions of Abrahamson *et al.* (2016) ground-motion model (GMM) were extracted from the probabilistic seismic hazard code available at https://github.com/usgs/nshmp-haz (last accessed September 2019). The unpublished manuscript by M. D. Petersen, A. M. Shumway, P. M. Powers, C. S. Mueller, M. P. Moschetti, A. D. Frankel, S. Rezaeian, D. E. McNamara, N. Luco, O. S. Boyd, K. S. Rukstales, K. S. Jaiswal, E. M. Thompson, S. M. Hoover, B. S. Clayton, E. H. Field, and Y. Zeng (2019), "2018 update of the U.S. National Seismic Hazard Model: Overview of model and implications," submitted to *Earthq. Spectra*.

Acknowledgments

The authors thank Erin Wirth and two anonymous reviewers for providing useful feedback on this work. The authors thank Jim Smith, Jason de Cristofaro, David Nget, Amanda Michaels, John Paskievitch, Cyrus Read, Fiona Eberhardt, and Adria McClain for leading and participating in the deployment of a temporary deployment of seismic instruments in the Cook Inlet region, following the 30 November 2018 M_w 7.1 Anchorage earthquake. This analysis and the aftershock deployment were supported by the U.S. Geological Survey (USGS) Earthquake Hazards Program. The facilities of Incorporated Research Institutions for Seismology (IRIS) Data Services, and specifically the IRIS Data Management Center, were used for access to waveforms, related metadata, and/or derived products used in this study. IRIS Data Services are funded through the Seismological Facilities for the Advancement of Geoscience and EarthScope (SAGE) Proposal of the National Science Foundation under Cooperative Agreement EAR-1261681.

References

Abrahamson, N., N. Gregor, and K. Addo (2016). BC Hydro ground motion prediction equations for subduction earthquakes, *Earthq. Spectra* **32,** no. 1, 23–44.

Abrahamson, N. A., W. J. Silva, and R. Kamai (2014). Summary of the ASK14 ground motion relation for active crustal regions, *Earthq. Spectra* **30,** no. 3, 1025–1055.

Aki, K. (1993). Local site effects on weak and strong ground motion, *Tectonophysics* **218,** nos. 1/3, 93–111.

Ancheta, T. D., R. B. Darragh, J. P. Stewart, E. Seyhan, W. J. Silva, B. S. J. Chiou, K. E. Wooddell, R. W. Graves, A. R. Kottke, D. M. Boore, and T. Kishida (2014). NGA-West2 database, *Earthq. Spectra* **30,** no. 3, 989–1005.

Anderson, J. G., Y. Lee, Y. Zeng, and S. Day (1996). Control of strong motion by the upper 30 meters, *Bull. Seismol. Soc. Am.* **86,** no. 6, 1749–1759.

Andrews, D. J. (1986). Objective determination of source parameters and similarity of earthquakes of different size, *Earthq. Source Mech.* **37,** 259–267.

Al Atik, L., N. Abrahamson, J. J. Bommer, F. Scherbaum, F. Cotton, and N. Kuehn (2010). The variability of ground-motion prediction models and its components, *Seismol. Res. Lett.* **81,** no. 5, 794–801.

Bindi, D., D. Spallarossa, and F. Pacor (2017). Between-event and between-station variability observed in the Fourier and response spectra domains: Comparison with seismological models, *Geophys. J. Int.* **210,** no. 2, 1092–1104.

Boore, D. M. (2010). Orientation-independent, nongeometric-mean measures of seismic intensity from two horizontal components of motion, *Bull. Seismol. Soc. Am.* **100,** no. 4, 1830–1835.

Boore, D. M., J. P. Stewart, E. Seyhan, and G. M. Atkinson (2014). NGA-West2 equations for predicting PGA, PGV, and 5% damped PSA for shallow crustal earthquakes, *Earthq. Spectra* **30,** no. 3, 1057–1085.

Borcherdt, R. D. (1970). Effects of local geology on ground motion near San Francisco Bay, *Bull. Seismol. Soc. Am.* **60,** no. 1, 29–61.

Bowden, D. C., and V. C. Tsai (2017). Earthquake ground motion amplification for surface waves, *Geophys. Res. Lett.* **44,** no. 1, 121–127.

Boyd, O. S., D. E. McNamara, S. Hartzell, and G. Choy (2017). Influence of lithostatic stress on earthquake stress drops in North America, *Bull. Seismol. Soc. Am.* **107,** no. 2, 856–868.

Campbell, K. W., and Y. Bozorgnia (2014). NGA-West2 ground motion model for the average horizontal components of PGA, PGV, and 5% damped linear acceleration response spectra, *Earthq. Spectra* **30,** no. 3, 1087–1115.

Çelebi, M. (2006). Recorded earthquake responses from the integrated seismic monitoring network of the Atwood Building, Anchorage, Alaska, *Earthq. Spectra* **22,** no. 4, 847–864.

Çelebi, M. (2019). Highlights of a cursory study of behavior of three instrumented buildings during the Mw7.1 Anchorage, Alaska, earthquake of November 30, 2018, *Seismol. Res. Lett.* doi: 10.1785/0220190220.

Chang, S. W., A. D. Frankel, and C. S. Weaver (2014). Report on workshop to incorporate basin response in the design of tall buildings in the puget sound region, Washington, *U.S. Geol. Surv. Open-File Rept. 2014-1196*, 28 pp., doi: 10.3133/ofr20141196.

Chiou, B. S. J., and R. R. Youngs (2014). Update of the Chiou and Youngs NGA model for the average horizontal component of peak ground motion and response spectra, *Earthq. Spectra* **30,** no. 3, 1117–1153.

Choi, Y., J. P. Stewart, and R. W. Graves (2005). Empirical model for basin effects accounts for basin depth and source location, *Bull. Seismol. Soc. Am.* **95,** no. 4, 1412–1427.

Davis, P. M., J. L. Rubinstein, K. H. Liu, S. S. Gao, and L. Knopoff (2000). Northridge earthquake damage caused by geologic focusing of seismic waves, *Science* **289,** no. 5485, 1746–1750.

Day, S. M., R. Graves, J. Bielak, D. Dreger, S. Larsen, K. B. Olsen, A. Pitarka, and L. Ramirez-Guzman (2008). Model for basin effects on long-period response spectra in southern California, *Earthq. Spectra* **24,** no. 1, 257–277.

Denolle, M. A., H. Miyake, S. Nakagawa, N. Hirata, and G. C. Beroza (2014). Long-period seismic amplification in the Kanto Basin from the ambient seismic field, *Geophys. Res. Lett.* **41,** no. 7, 2319–2325.

Earle, P. S., D. J. Wald, K. S. Jaiswal, T. I. Allen, M. G. Hearne, K. D. Marano, A. J. Hotovec, and J. M. Fee (2009). Prompt Assessment of Global Earthquakes for Response (PAGER): A system for rapidly determining the impact of earthquakes worldwide, *U.S. Geol. Surv. Open-File Rept. 2009-1131*, 15 pp.

Feng, L., and M. H. Ritzwoller (2017). The effect of sedimentary basins on surface waves that pass through them, *Geophys. J. Int.* **211,** no. 1, 572–592.

Franke, K. W., R. D. Koehler, C. Z. Beyzaei, A. Cabas, I. Pierce, A. W. Stuedlein, and Z. Yang (2018). Geotechnical engineering reconnaissance of the 30 November 2018 Mw 7.0 Anchorage, Alaska Earthquake, Version 1.0, *GEER Rept. GEER-059*, doi: 10.18118/G6P07F, 50 pp.

Frankel, A. (1993). Three-dimensional simulations of ground motions in the San Bernardino Valley, California, for hypothetical earthquakes on the San Andreas Fault, *Bull. Seismol. Soc. Am.* **83,** no. 4, 1020–1041.

Frankel, A., R. Chen, M. Petersen, M. Moschetti, and B. Sherrod (2015). 2014 update of the Pacific Northwest portion of the U.S. National Seismic Hazard Maps, *Earthq. Spectra* **31,** no. S1, S131–S148.

Frankel, A., W. Stephenson, and D. Carver (2009). Sedimentary basin effects in Seattle, Washington: Ground-motion observations and 3D simulations, *Bull. Seismol. Soc. Am.* **99,** no. 3, 1579–1611.

Frankel, A., E. Wirth, N. Marafi, J. Vidale, and W. Stephenson (2018). Broadband synthetic seismograms for magnitude 9 earthquakes on the Cascadia megathrust based on 3D simulations and stochastic synthetics, Part 1: Methodology and overall results, *Bull. Seismol. Soc. Am.* **108,** no. 5A, 2347–2369.

Frankel, A. D., D. L. Carver, and R. A. Williams (2002). Nonlinear and linear site response and basin effects in Seattle for the M 6.8 Nisqually, Washington, earthquake, *Bull. Seismol. Soc. Am.* **92,** no. 6, 2090–2109.

Garcia, D., D. J. Wald, and M. G. Hearne (2012). A global earthquake discrimination scheme to optimize ground-motion prediction equation selection, *Bull. Seismol. Soc. Am.* **102,** no. 1, 185–203.

Geli, L., P. Y. Bard, and B. Jullien (1988). The effect of topography on earthquake ground motion: A review and new results, *Bull. Seismol. Soc. Am.* **78,** no. 1, 42–63.

Goulet, C. A., T. Kishida, T. D. Ancheta, C. H. Cramer, R. B. Darragh, W. J. Silva, Y. M. A. Hashash, J. Harmon, J. P. Stewart, K. E. Wooddell, and R. R. Youngs (2014). PEER NGA-East database, *PEER Rept. 2014/17*, Pacific Earthquake Engineering Research Center, Berkeley, California, 124 pp.

Guy, M. R., J. M. Patton, J. Fee, M. Hearne, E. Martinez, D. Ketchum, C. Worden, V. Quitoriano, E. Hunter, G. Smoczyk, and S. Schwarz (2015). National Earthquake Information Center systems overview and integration, *U.S. Geol. Surv. Open-File Rept. 2015-1120*, 25 pp., doi: 10.3133/ofr20151120.

Hartzell, S., E. Cranswick, A. Frankel, D. Carver, and M. Meremonte (1997). Variability of site response in the Los Angeles urban area, *Bull. Seismol. Soc. Am.* **87,** no. 6, 1377–1400.

Hayes, G. P., G. L. Moore, D. E. Portner, M. Hearne, H. Flamme, M. Furtney, and G. M. Smoczyk (2018). Slab2, a comprehensive subduction zone geometry model, *Science* **362,** no. 6410, 58–61.

Hearne, M., E. M. Thompson, H. Schovanec, J. Rekoske, B. T. Aagaard, and C. B. Worden (2019). *USGS Automated Ground Motion Processing Software*, doi: 10.5066/P9ANQXN3.

Kawase, H. (1996). The cause of the damage belt in Kobe: "The basin-edge effect," constructive interference of the direct S-wave with the basin-induced diffracted/Rayleigh waves, *Seismol. Res. Lett.* **67,** no. 5, 25–34.

Kennett, B. L. N., and E. R. Engdahl (1991). Traveltimes for global earthquake location and phase identification, *Geophys. J. Int.* **105,** no. 2, 429–465.

Krischer, L., T. Megies, R. Barsch, M. Beyreuther, T. Lecocq, C. Caudron, and J. Wassermann (2015) ObsPy: A bridge for seismology into the scientific Python ecosystem, *Comp. Sci. Discov.* **8,** no. 1, 014003.

Landwehr, N., N. M. Kuehn, T. Scheffer, and N. Abrahamson (2016). A nonergodic ground-motion model for California with spatially varying coefficients, *Bull. Seismol. Soc. Am.* **106,** no. 6, 2574–2583.

Li, J., G. A. Abers, Y. Kim, and D. Christensen (2013). Alaska megathrust 1: Seismicity 43 years after the great 1964 Alaska megathrust earthquake, *J. Geophys. Res.* **118,** no. 9, 4861–4871.

McNamara, D. E., E. Wolin, P. M. Powers, A. M. Shumway, M. P. Moschetti, J. Rekoske, E. Thompson, C. S. Mueller, and M. D. Petersen (2019). Evaluation of ground motion models for USGS seismic hazard forecasts: 2018 Anchorage Alaska Mw 7.1 subduction zone earthquake sequence, *Seismol. Res. Lett.* doi: 10.1785/0220190188.

Moschetti, M. P., S. Hartzell, L. Ramírez-Guzmán, A. D. Frankel, S. J. Angster, and W. J. Stephenson (2017). 3D ground-motion simulations of Mw 7 earthquakes on the Salt Lake City segment of the Wasatch fault zone: Variability of long-period ($T \geq 1$ s) ground motions and sensitivity to kinematic rupture parameters, *Bull. Seismol. Soc. Am.* **107,** no. 4, 1704–1723.

Moschetti, M. P., E. M. Thompson, P. M. Powers, S. M. Hoover, and D. E. McNamara (2018). Ground motions from induced earthquakes in Oklahoma and Kansas, *Seismol. Res. Lett.* **90,** no. 1, 160–170.

Müller, R. D., M. Sdrolias, C. Gaina, and W. R. Roest (2008). Age, spreading rates and spreading symmetry of the world's ocean crust, *Geochem. Geophys. Geosys.* **9,** Q04006, doi: 10.1029/2007GC001743.

Nweke, C. C., P. Wang, S. J. Brandenberg, and J. P. Stewart (2018). *Reconsidering Basin Effects in Ergodic Site Response Models*, UCLA publication, Los Angeles, California, available at https://escholarship.org/uc/item/6048v74k (last accessed August 2019).

Olsen, K. B. (2000). Site amplification in the Los Angeles basin from three-dimensional modeling of ground motion, *Bull. Seismol. Soc. Am.* **90,** no. 6B, S77–S94.

Pinheiro, J., D. Bates, S. DebRoy, D. Sarkar, and Development Core Team (2013). nlme: Linear and nonlinear mixed effects models, *R package version 3*, 1–113.

Rekoske, J., M. P. Moschetti, E. M. Thompson, M. Hearne, and C. Tape (2019). Database of ground motions from in-slab earthquakes near Anchorage, Alaska, 2008–2019, Center for Engineering Strong Motion Data (CESMD), doi: 10.5066/P9Y491AY.

Rennolet, S. B., M. P. Moschetti, E. M. Thompson, and W. L. Yeck, (2018). A flatfile of ground motion intensity measurements from induced earthquakes in Oklahoma and Kansas, *Earthq. Spectra* **34,** no. 1, 1–20.

Rodriguez-Marek, A., E. M. Rathje, J. J. Bommer, F. Scherbaum, and P. J. Stafford (2014). Application of single-station sigma and site-response characterization in a probabilistic seismic-hazard analysis for a new nuclear site, *Bull. Seismol. Soc. Am.* **104,** no. 4, 1601–1619.

Shapiro, N. M., K. B. Olsen, and S. K. Singh (2000). Wave-guide effects in subduction zones: Evidence from three-dimensional modeling, *Geophys. Res. Lett.* **27,** no. 3, 433–436.

Shellenbaum, D. P., L. J. Gregersen, and P. R. Delaney (2010) *Top Mesozoic Unconformity Depth Map of the Cook Inlet Basin, Alaska: Report of Investigations RI 2010-2*, Alaska Division of Geological & Geophysical Surveys, Fairbanks, Alaska.

Smith, K., and C. Tape (2019). Seismic response of Cook Inlet sedimentary basin, southern Alaska, *Seismol. Res. Lett.* doi: 10.1785/0220190205.

Spudich, P., M. Hellweg, and W. H. K. Lee (1996). Directional topographic site response at Tarzana observed in aftershocks of the 1994 Northridge, California, earthquake: Implications for mainshock motions, *Bull. Seismol. Soc. Am.* **86,** no. 1B, S193–S208.

Tape, C., D. Christensen, M. M. Moore-Driskell, J. Sweet, and K. Smith (2017). Southern Alaska Lithosphere and Mantle Observation Network (SALMON): A seismic experiment covering the active arc by road, boat, plane, and helicopter, *Seismol. Res. Lett.* **88,** no. 4, 1185–1202.

Thompson, E. M., and D. J. Wald (2016). Uncertainty in VS30-based site response, *Bull. Seismol. Soc. Am.* **106,** no. 2, 453–463.

Thompson, E. M., B. Aaagaard, M. Hearne, H. Schovanec, J. Rekoske, D. J. Wald, E. Kalkan, J. H. Steidl, and A. R. Kottke (2019). Community-supported ground motion processing software, presented at the *Annual Meeting of the Seismological Society of America*, Seattle, Washington, April 2019.

Wald, D. J., and T. I. Allen (2007). Topographic slope as a proxy for seismic site conditions and amplification, *Bull. Seismol. Soc. Am.* **97,** no. 5, 1379–1395, doi: 10.1785/0120060267.

Wessel, P., W. H. F. Smith, R. Scharroo, J. F. Luis, and F. Wobbe (2013). Generic Mapping Tools: Improved version released, *EOS Trans. AGU* **94,** 409–410.

Wesson, R. L., O. S. Boyd, C. S. Mueller, C. G. Bufe, A. D. Frankel, and M. D. Petersen (2007). Revision of time-independent probabilistic seismic hazard maps for Alaska, *U.S. Geol. Surv. Open-File Rept. 2007-1043*, doi: 10.3133/ofr20071043.

Wirth, E. A., S. W. Chang, and A. D. Frankel (2018). 2018 report on incorporating sedimentary basin response into the design of tall buildings in Seattle, Washington, *U.S. Geol. Surv. Open-File Rept. 2018-1149*, 19 pp.

Wirth, E. A., A. D. Frankel, N. Marafi, J. E. Vidale, and W. J. Stephenson (2018). Broadband synthetic seismograms for magnitude 9 earthquakes on the Cascadia megathrust based on 3D simulations and stochastic synthetics, Part 2: Rupture parameters and variability, *Bull. Seismol. Soc. Am.* **108,** no. 5A, 2370–2388.

Wirth, E. A., J. E. Vidale, A. D. Frankel, T. L. Pratt, N. Marafi, M. Thompson, and W. J. Stephenson (2019). Source-dependent amplification of earthquake ground motions in deep sedimentary basins, *Geophys. Res. Lett.* **46,** 6443–6450.

Wooddell, K. E., and N. A. Abrahamson (2014). Classification of main shocks and aftershocks in the NGA-West2 database, *Earthq. Spectra* **30,** no. 3, 1257–1267.

Wooddell, K. E., and N. A. Abrahamson (2019). Overcoming limitations of ergodic GMPEs: Properly separating earthquake source and path terms, presented at the *2019 Annual Meeting of the Seismological Society of America*, Seattle, Washington, April 2019.

Manuscript received 12 July 2019
Published online 20 November 2019